The Astrophysical Journal Letters, 1000:L31 (9pp), 2026 March 20 https://doi.org/10.3847/2041-8213/ae4c84
© 2026. The Author(s). Published by the American Astronomical Society.
OPEN ACCESS

An Origin of Radially Aligned Filaments in Hub-filament Systems

Shingo Nozaki[1] and Shu-ichiro Inutsuka[2]
[1] Department of Earth and Planetary Sciences, Faculty of Science, Kyushu University, Nishi-ku, Fukuoka 819-0395, Japan; nozaki.shingo.307@s.kyushu-u.ac.jp
[2] Department of Physics, Graduate School of Science, Nagoya University, Furo-cho, Chikusa-ku, Nagoya, Aichi 464-8602, Japan
Received 2026 January 19; revised 2026 February 27; accepted 2026 March 3; published 2026 March 18

Abstract

Recent observations have identified hub-filament systems (HFSs) as the primary formation sites of massive stars and star clusters. Some HFSs are characterized by multiple filaments aligned radially toward a central high-density hub. However, the physical origin of radially aligned filaments remains unknown. Here, we propose a new formation mechanism of HFSs driven by the interaction of a fast magnetohydrodynamic shock with a molecular cloud characterized by an hourglass-shaped magnetic field and density inhomogeneity. Our three-dimensional magnetohydrodynamic simulations show that the shock propagation leads to the formation of radially aligned filamentary structures with line masses slightly above the thermally critical line mass and lengths of 1–3 pc and widths of 0.06−0.08 pc. High-density filamentary gas ($n_{\rm H_2} \sim 10^4$ cm^{-3}) selectively exhibits inward velocities of 1–4 km s^{-1} that increase toward the hub center, while the ambient low-density interfilament gas retains low velocities regardless of the radius. Mass accretion onto the hub is channeled through dense filaments. The filament formation is driven by oblique shocks generated at the bent magnetic field lines. The resulting postshock amplification of the tangential magnetic field induces a magnetically guided inflow. The shock–interface interaction amplifies density perturbations, resembling Richtmyer–Meshkov instability modes, which promotes the fragmentation of the shocked layer into multiple filaments. The process studied in this Letter explains both the morphology of radially aligned filaments and the selective mass accretion observed in HFSs. In our simulation, the resulting star formation efficiency (SFE) is ∼4%, suggesting that the shock-driven evolution limits the SFE to only a few percent.

Unified Astronomy Thesaurus concepts: Magnetohydrodynamics (1964); Star formation (1569); Interstellar medium (847); Interstellar dynamics (839)

1. Introduction

Filamentary structures in molecular clouds are the primary sites of star formation. Among filamentary structures, the hub-filament system (HFS), consisting of filaments radially converging to a central dense hub, is a key site for cluster and high-mass star formation (e.g., P. C. Myers 2009; M. S. N. Kumar et al. 2020). Observations using Herschel, Spitzer, and Atacama Large Millimeter/submillimeter Array have revealed such parsec-scale systems in various star-forming regions. For example, in the Mon R2 cloud, a network of filaments aligns radially toward the hub center (M. S. N. Kumar et al. 2022). Similar structures are identified in both high- and low-mass star-forming regions (e.g., L. K. Dewangan et al. 2025), suggesting their universality in clustered star formation. While magnetic fields and gas kinematics in HFSs have been observationally characterized (e.g., J.-W. Wang et al. 2019, 2020a, 2020b; J. Hwang et al. 2022; J. W. Zhou et al. 2023), the physical origin of the HFS morphology remains poorly understood.

Theoretical studies have proposed various mechanisms for filament formation. T. Inoue et al. (2018) showed, using simulations of shock–cloud interactions, that a shock propagating perpendicular to the magnetic field generates complex filamentary structures via the formation of oblique shocks. D. Abe et al. (2021) revealed that formation mechanisms can be classified into four types based on the field-flow orientation, indicating that the interaction between the shock and the magnetic field plays a crucial role in filament formation. On the other hand, as attempts to understand the HFS formation process, numerical simulations focusing on individual filament–filament collisions (e.g., R. Kashiwagi et al. 2024) and gravitational structure formation models based on global hierarchical collapse (e.g., E. Vázquez-Semadeni et al. 2025) have been proposed. However, the formation of distinct radially aligned filaments converging to a central hub, as observed in HFSs, has not yet been reproduced. While previous shock–cloud interaction studies assumed a shock propagating perpendicular to a uniform magnetic field, the effect of field curvature has not been considered. Given that molecular clouds are threaded by hourglass-shaped magnetic fields due to self-gravity, investigating the interaction between a shock and such curved field geometries is crucial for understanding the origin of HFSs.

In this Letter, we investigate the interaction of a fast-mode shock with a molecular cloud characterized by an hourglass-shaped magnetic field and density inhomogeneity, using three-dimensional ideal magnetohydrodynamic (MHD) simulations. We demonstrate that the shock–cloud interaction generates multiple filaments radially aligned toward a central hub. Based on these results, we propose a new scenario for HFSs driven by external shocks, such as those from supernova remnants or expanding H II regions, interacting with the preexisting curved magnetic field.

2. Numerical Settings

To investigate the formation mechanism of the HFSs, we have performed three-dimensional ideal MHD simulations using the adaptive mesh refinement code SFUMATO (T. Matsumoto 2007; T. Matsumoto et al. 2015; H. Fukushima & H. Yajima 2021;

Original content from this work may be used under the terms of the Creative Commons Attribution 4.0 licence. Any further distribution of this work must maintain attribution to the author(s) and the title of the work, journal citation and DOI.

S. Nozaki et al. 2025), which solves the equations of ideal MHD with self-gravity (see also T. Matsumoto 2007 for the basic equations). The heating and cooling processes include gas–dust energy exchange, line emission, and chemical heating, implemented with a simplified chemical network (H. Fukushima et al. 2020; H. Fukushima & H. Yajima 2021). To model the interaction between a molecular cloud and an external shock originating from a supernova remnant, we consider a cloud placed within a cube simulation box with a side length of 10 pc. The background number density in the computational domain is initially set to $n_{\rm bg} = 1.01 \times 10^2\,{\rm cm}^{-3}$, comparable to the typical density of a giant molecular cloud envelope (e.g., M. Heyer & T. M. Dame 2015). We adopt the initial condition of a cloud that is flattened along the z-direction. The density distribution smoothly connects to the background and is given by

$$n_{\rm H_2} = n_{\rm bg} + n_{\rm bg}\,(A_{\rm max} - 1) \times \left[1 + \frac{x^2 + y^2 + ((z - z_{\rm off})/\alpha)^2}{R_{\rm flat}^2}\right]^{-2}, \quad (1)$$

where $A_{\rm max}$ is the peak-to-background density contrast, set to $A_{\rm max} = 130$. The parameters α and $R_{\rm flat}$ characterize the degree of vertical flattening and the radius of the central flat region, set to $\alpha = 0.1$ and $R_{\rm flat} = 1.75$ pc, respectively. The vertical offset of the cloud center is set to $z_{\rm off} = +1.45$ pc. The total gas mass in the computational domain is $8.6 \times 10^3\,M_\odot$. The mass of the initial cloud, defined as gas with $n_{\rm H_2} > 1.02 \times 10^2\,{\rm cm}^{-3}$, is $4.8 \times 10^3\,M_\odot$. The initial magnetic field is uniform and oriented along the z-axis with a strength of $B_0 = 15\,\mu$G, consistent with typical values observed in nearby molecular clouds (R. M. Crutcher et al. 2010; K. Pattle et al. 2023). The corresponding mass-to-flux ratio of the entire computational domain is 1.9, indicating that the cloud is slightly supercritical. The base grid consists of 128^3 cells. At the finest refinement level ($l_{\rm max} = 4$), the cell width is $\Delta x = 9.8 \times 10^{-3}$ pc, which resolves the local Jeans length by more than five cells. Sink particles are introduced when the gas density exceeds $n_{\rm H_2,thr} = 1 \times 10^5\,{\rm cm}^{-3}$ in order to follow the long-term evolution of the cloud.

A planar shock propagating in the negative z-direction is injected from the upper boundary ($z = +5$ pc) of the computational domain. As for fluid boundary conditions, the $z = +5$ pc plane is treated as a fixed inflow boundary, while the remaining five boundaries are set to free boundaries. At the fixed boundary, an inflow velocity of $v = (0, 0, v_{\rm shock})$ is imposed, with $v_{\rm shock} = -5.0\,{\rm km\,s}^{-1}$. All other physical quantities at this boundary are fixed to their initial ambient values outside the cloud, except for the gas pressure, enhanced to 5×10^2 times the ambient pressure in order to drive the shock. This inflow velocity corresponds to sonic and background Alfvénic Mach numbers of approximately 27 and 2.3, respectively, for a 10 K molecular gas, exceeding the fast-magnetosonic speed. Following T. Matsumoto et al. (2015), we initialize a turbulent velocity field throughout the computational domain with an rms Mach number of $\mathcal{M}_{\rm rms} = 2$, allowed to decay without continuous driving.

Before the shock reaches the molecular cloud, the initially uniform magnetic field aligned with the z-axis becomes slightly pinched near the cloud center due to gravitational contraction, forming a weak hourglass-shaped magnetic-field morphology. Such hourglass-shaped magnetic-field structures on molecular cloud scales have been reported in observations of massive star-forming regions (e.g., M. T. Beltrán et al. 2019). In the fiducial ($\psi = 0°$) configuration, the fast-mode shock propagates nearly parallel to the large-scale magnetic field along the z-direction. The initially imposed turbulent velocity field introduces weak inhomogeneity in the density distribution of the molecular cloud prior to the shock impact. The simulation is evolved up to 0.5 Myr after the shock reaches the cloud, which is sufficient to capture the formation of the HFS and its early dynamical evolution. Extending the calculation to later times would require prohibitively small time steps, mainly due to the high Alfvén speeds and outflow velocities that are generated by the shock–cloud interaction. This would lead to a substantial increase in computational cost.

In addition to adopting the fiducial configuration ($\psi = 0°$) as the reference model, we performed supplementary simulations in which the magnetized cloud system is rotated as a whole, while the shock propagation direction is kept fixed along the z-axis. This setup introduces relative inclination angles of $\psi = 10°$, $15°$, $20°$, and $30°$ between the shock direction and the magnetic field, compared to the fiducial $\psi = 0°$ case.

In this Letter, we focus on the $\psi = 0°$ model as a representative case to demonstrate the key physical processes, specifically at the epoch when the HFS is clearly established, while showing the $\psi = 15°$ and $30°$ models to assess the robustness of the morphology against deviations from the idealized geometry. A systematic parameter survey is deferred to future work.

3. Results

3.1. Formation of Radially Aligned Filaments

As shown in the left panel of Figure 1, an HFS develops when a fast-mode shock reaches the central region of the cloud with an hourglass-shaped magnetic field and weak density inhomogeneity introduced by turbulence. Multiple filaments with lengths of 1–3 pc extend radially from the central hub, exhibiting a spoke-like morphology. Their radial configuration and column densities are comparable to those observed in HFSs (e.g., M. S. N. Kumar et al. 2022; L. K. Dewangan et al. 2025).

We also show simulations in which the shock propagation direction is inclined by $\psi = 15°$ and $30°$ relative to the magnetic-field axis (Figure 1, right panels). In both cases, radially aligned filaments develop around the central hub. Although the overall symmetry decreases with increasing inclination angle, the tendency for filament alignment toward the hub is preserved. In the $\psi = 30°$ case, filament formation tends to be weaker on the side of the cloud that is struck first by the shock (the left side in $\psi = 30°$ panel of Figure 1), leading to a more asymmetric hub-filament morphology. This likely reflects the fact that the shock interacts with the cloud and the curved magnetic-field structure at different times and with different effective obliquities across the cloud. In the following analysis, we focus on the $\psi = 0°$ case, which provides the clearest illustration of the underlying mechanism.

We identified filamentary structures using DisPerSE (T. Sousbie 2011; T. Sousbie et al. 2011), as illustrated in Figure 2(a). The extraction was performed on logarithmic column density maps smoothed with a 2 pixel Gaussian kernel to suppress grid noise. We adopted a persistence threshold of 0.02 dex to detect faint structures (column density contrast

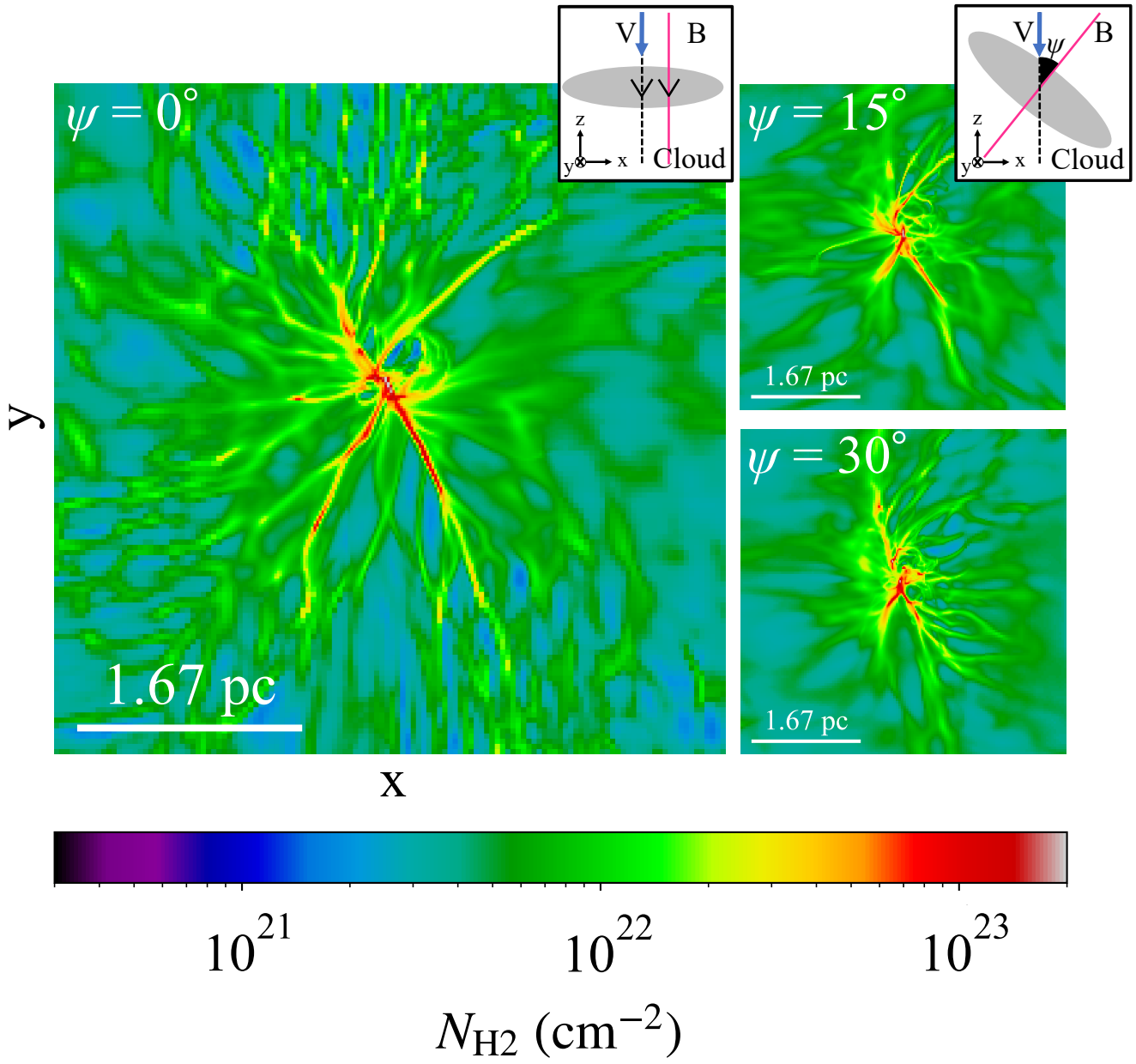

Figure 1. H_2 column density maps in the x–y plane at $t = 0.5$ Myr after the shock sweeps the cloud for different inclination angles ψ between the shock propagation direction and the magnetic-field axis. The panels show $\psi = 0°$, 15°, and 30°. The color scale represents the H_2 column density integrated along the z-axis. The box size is 5.0 pc on each side. Small inset schematics in each panel illustrate the definition of the inclination angle ψ (between the shock propagation direction and the magnetic-field axis) and the corresponding initial cloud-field geometry; the gray shape, magenta line, and blue arrow indicate the initial cloud density profile, magnetic-field direction, and shock propagation direction, respectively.

$\gtrsim$5%) while avoiding artifacts and removed unphysical segments. We measured the characteristic width directly from the column density map. Transverse profiles were sampled perpendicular to the extracted filament skeletons and stacked to construct a mean radial profile. Fitting this profile with a Gaussian plus a constant background yields a characteristic full width at half-maximum (FWHM) of ∼0.07 pc. Alternative estimators, including Plummer fitting with fixed $p = 2$ and direct half-maximum measurements (e.g., D. Arzoumanian et al. 2019), give consistent values in the range 0.06–0.08 pc. Using this measured width, we defined the filament region as the area within one FWHM radius from the filament skeleton. The total filament mass was obtained by integrating the column density over the entire filament network identified with DisPerSE. We derived a mean H_2 column density of 8×10^{21} cm^{-2} for the identified filaments. This value exceeds the star formation threshold suggested by P. André et al. (2010), indicating that the identified filaments represent a dense filamentary network capable of hosting active star formation. The corresponding line mass is $22\,M_\odot\,\mathrm{pc}^{-1}$, slightly above the thermal critical line mass at 10 K ($M_{\mathrm{line,cri}} \sim 16.8\,M_\odot\,\mathrm{pc}^{-1}$), suggesting that these filaments are in a mildly supercritical state.

To quantify the geometric alignment, we measured the deviation angle, $\Delta\theta$, defined between the local tangent of each filament and the radial vector originating from the hub center as in M. S. N. Kumar et al. (2022). As shown in Figure 2(b), the distribution of the mean deviation angle, $\langle\Delta\theta\rangle$, for

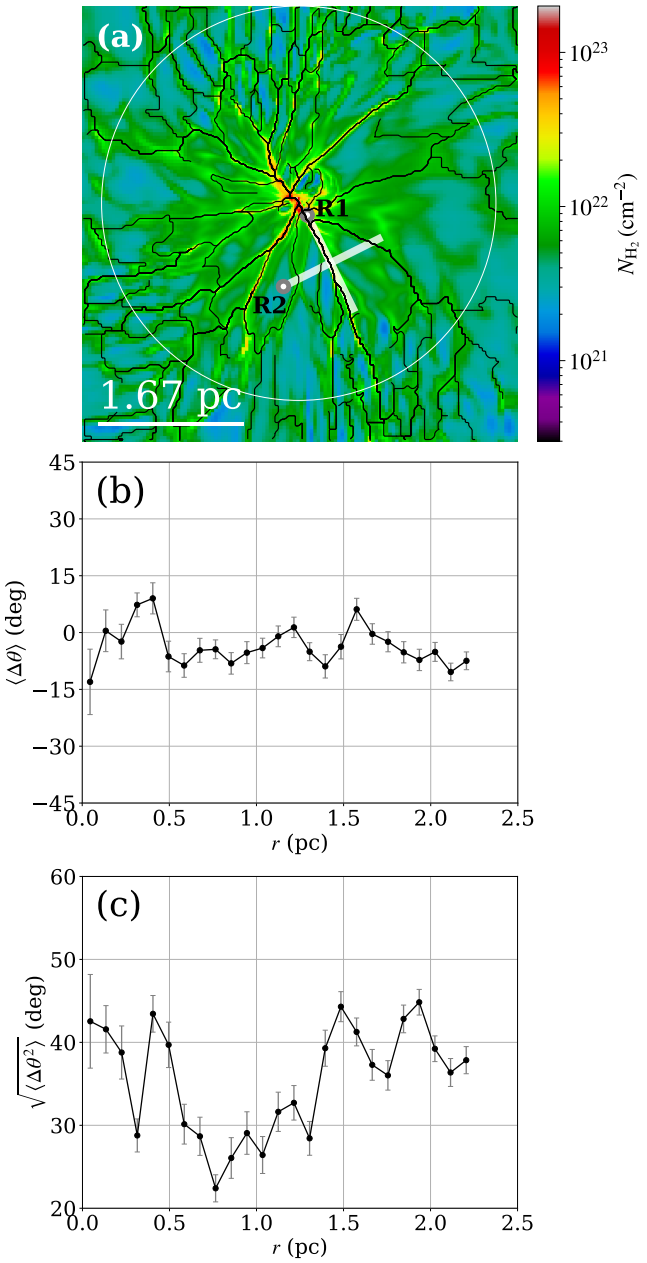

Figure 2. (a) H_2 column density map from the left panel of Figure 1, overlaid with filament skeletons identified using DisPerSE (T. Sousbie 2011; T. Sousbie et al. 2011). The lines labeled R1 and R2 denote cuts parallel and perpendicular to the filaments, respectively (see Figure 4 for details). The white circle (diameter of 4.5 pc) indicates the region centered on the density peak. (b)–(c) Radial profiles of the mean angle $\langle\Delta\theta\rangle$ (b) and the rms angle (c) of the filaments relative to the radial vector from the hub center. The hub center is defined as the column density peak, distinct from the geometric center of the simulation box. The angle $\Delta\theta$ ranges from $-90°$ to $90°$, where $0°$ corresponds to the radial direction. The plots cover the region within the white circle in (a). Error bars represent the standard errors.

filaments within a radius of 2.25 pc is tightly confined to the range of $-15°$ to $15°$, indicating that most filaments are closely aligned with the radial direction. As presented in Figure 2(c), the rms angles of the filaments relative to the radial vector fall within the range of $0°$–$45°$. These values are consistently lower than the dispersion expected for a random orientation (rms $\sim 52°$), confirming a significant tendency toward radial alignment. These statistical results quantitatively substantiate the formation of the radially aligned HFS visualized in the left panel of Figure 1, showing a remarkable agreement with M. S. N. Kumar et al. (2022).

3.2. Velocity Structure of the Hub-filament System

Figure 3(a) reveals a clear kinematic distinction between the dense and diffuse gas components. The high-density gas ($n_{H_2} \sim 3.0 \times 10^4\,\mathrm{cm^{-3}}$, corresponding to filaments) exhibits high inward velocities ($V_r \sim -4$ to $-1\,\mathrm{km\,s^{-1}}$) that increase toward the hub center. In contrast, the ambient low-density gas retains low velocities ($V_r \sim -1$ to $+0.5\,\mathrm{km\,s^{-1}}$) regardless of the radius. Exceptions are found in minor diffuse components. Postshock gas located downstream of the cloud is accelerated by pressure gradients along folded magnetic-field lines, exhibiting rapid inflow ($V_r < -1\,\mathrm{km\,s^{-1}}$). In addition, gas near the hub shows localized outward motions ($V_r > 1\,\mathrm{km\,s^{-1}}$) driven by magnetic tension from the distorted hourglass-shaped field. Despite these local exceptions, the overall kinematic segregation between the dense and diffuse gas agrees with the interpretations of observations for high-speed inflows along filaments in HFSs (e.g., N. Peretto et al. 2014; Y. Shimajiri et al. 2019; S. P. Treviño-Morales et al. 2019).

Figure 3(b) presents the median density-weighted velocity dispersion σ_{v_z} along the z-axis, corresponding to the shock propagation direction. We find that σ_{v_z} tends to increase toward the outer radii, consistent with the observational trends reported by N. Peretto et al. (2023). The relatively low dispersion near the center suggests that ordered radial inflow dominates over random turbulent motions in the dense hub region. Combined with the radial velocity analysis, these results indicate that, driven by the shock–cloud interaction, mass accretion is selectively channeled through high-density filaments rather than occurring uniformly from the entire cloud, leaving the ambient gas dynamically detached from the primary inflow.

For comparison with observations, Figure 3(c1) shows the projected dense gas distribution and its corresponding line-of-sight velocity field, and Figure 3(c2) presents the associated position–velocity (PV) diagram. Only gas above the column density threshold of $8 \times 10^{21}\,\mathrm{cm^{-2}}$, comparable to the mean column density of the identified filaments, is included. The dense radially aligned filaments exhibit a systematic variation of $V_{\mathrm{los},z-}$ across the HFS, with a velocity difference of up to $\sim 10\,\mathrm{km\,s^{-1}}$ across the 5 pc region. This large-scale velocity gradient produces a clear V-shaped pattern in the PV diagram (Figure 3(c2)), reflecting the shock-driven reorganization of the velocity field. The overall PV morphology closely resembles the V-shaped signatures reported in high-mass protoclusters and HFSs (e.g., R. H. Álvarez-Gutiérrez et al. 2024; J. Salinas et al. 2025; N. A. Sandoval-Garrido et al. 2025). In contrast to some observed regions that exhibit multiple velocity components, our model produces a single coherent V-shaped feature, consistent with a single shock interaction from one direction.

3.3. Formation Mechanism of the Hub-filament System

Figure 4(R1) presents the distributions of density, velocity, and magnetic fields in a slice along the axis of a single filament with a width of ~ 0.1 pc. Across the dense filamentary structure, distinct refraction of magnetic-field vectors and field strength enhancement are evident. This signature is characteristic of an oblique fast-mode shock on the hourglass-

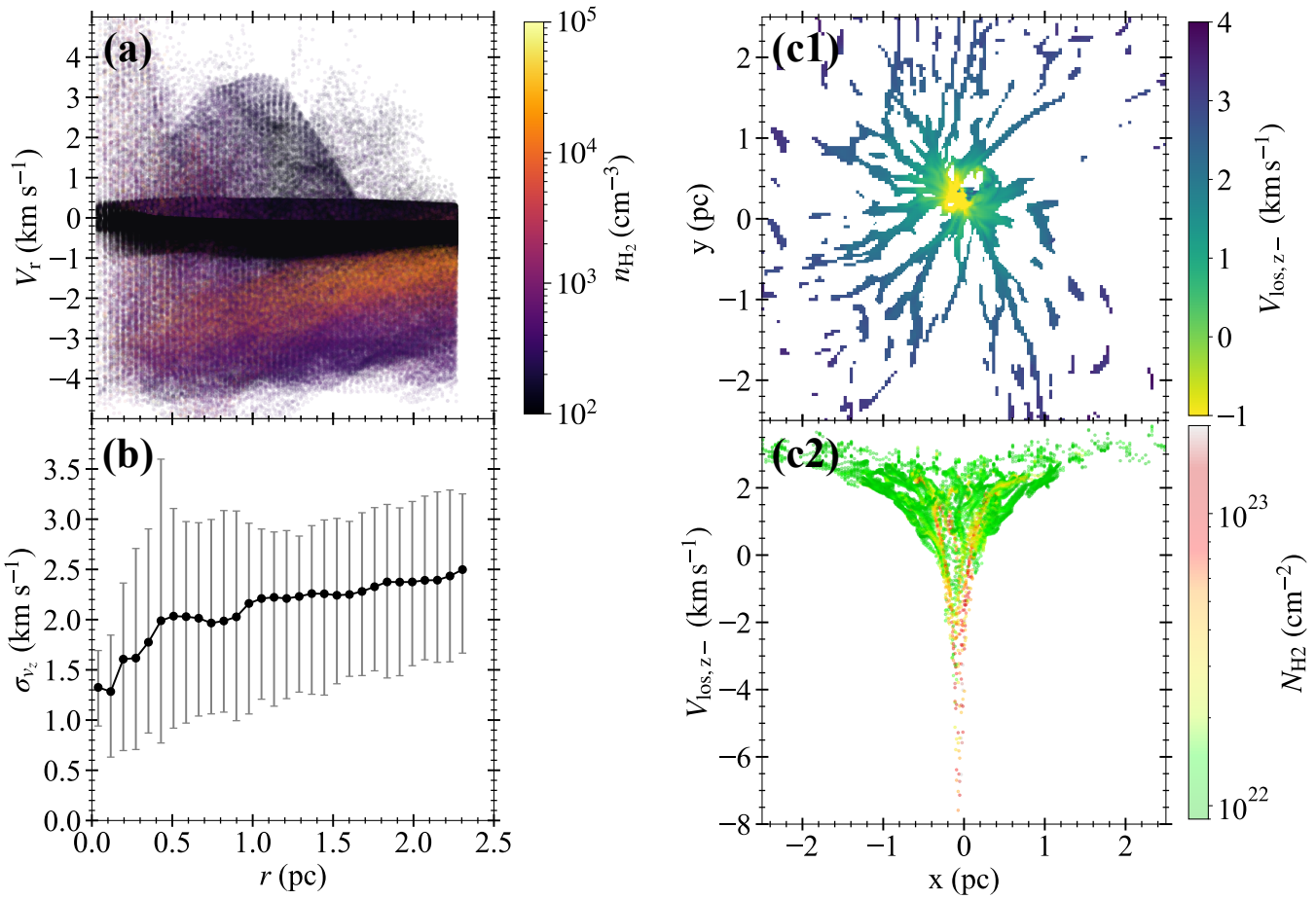

Figure 3. Velocity structure of the HFS 0.5 Myr after the shock impact. (a) Radial velocity V_r plotted as a function of the cylindrical radius r from the hub center. V_r and r are defined in a cylindrical coordinate system aligned with the z-axis. The color of each point corresponds to the H_2 number density. Only cells within a cylindrical radius of $r = 2.25$ pc are plotted. (b) Median of the density-weighted velocity dispersion σ_{v_z} along the z-axis as a function of r. Error bars indicate the 95% confidence intervals. Note that in both panels, the hub center is defined as the position of the peak gas density at this epoch and does not coincide with the origin of the computational domain. (c1 and c2) Observationally motivated kinematic maps constructed from the same snapshot as in the left panel of Figure 1. (c1) Column-density-selected line-of-sight velocity map. Only regions with $N_{H_2} > 8 \times 10^{21}$ cm^{-2}, corresponding approximately to the mean column density of the identified filaments, are included. The line-of-sight velocity components are measured along the z-axis from an observer located at $z = -\infty$ and are shown in the laboratory frame. (c2) Position–velocity (PV) diagram showing the line-of-sight velocity $V_{los,z-}$ as a function of the projected x-coordinate, weighted by the column density.

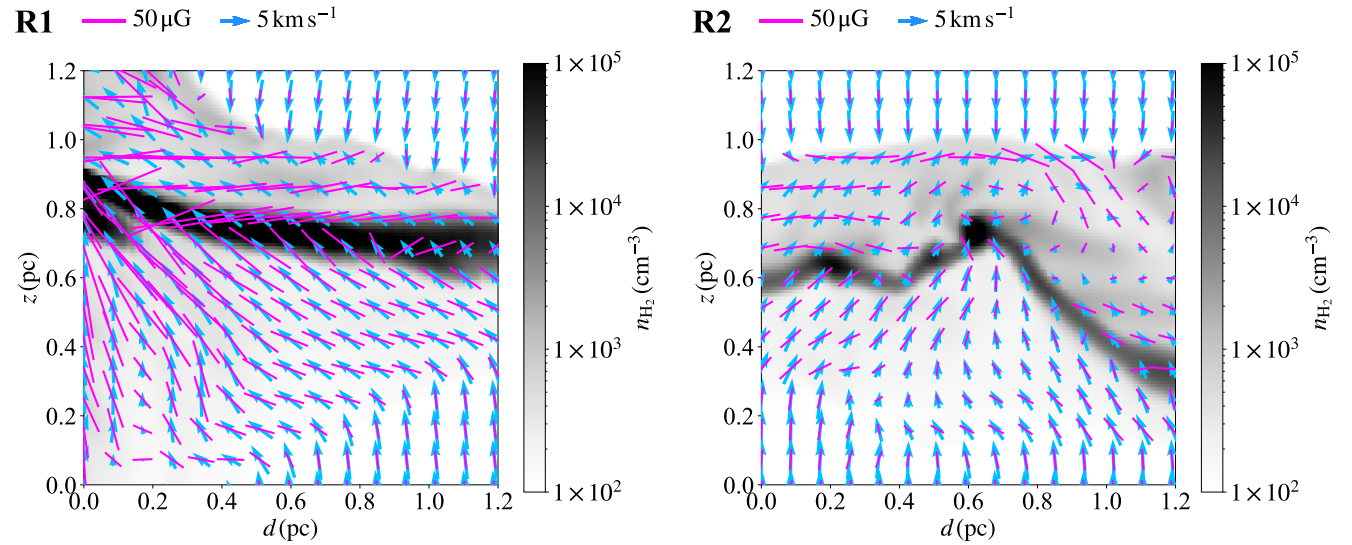

Figure 4. Distributions of density, velocity, and magnetic fields in slices along the filament axis (R1) and across the filament width (R2). The positions of these cuts are indicated by white lines in Figure 2(a). Magenta bars and blue arrows denote the magnetic field and velocity vectors, respectively. The velocity vectors are presented in the shock rest frame ($v_{shock} = -5$ km s^{-1}). The grayscale represents the H_2 number density. The horizontal axis d corresponds to the distance along the cut, where the white circle with a gray outline in Figure 2(a) marks the starting points ($d = 0$). The vertical axis z represents the vertical position within the slice.

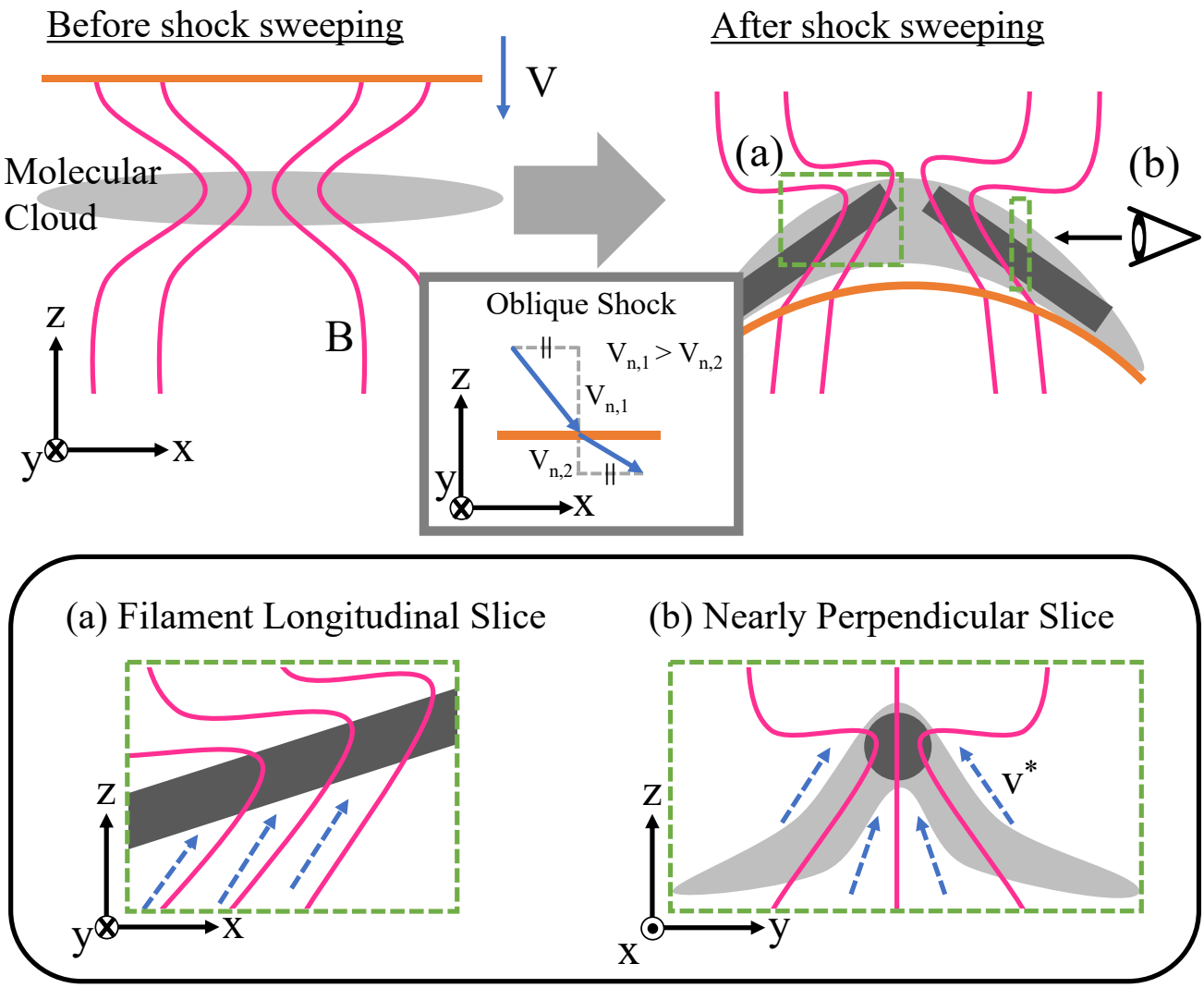

Figure 5. Schematic illustration of a fast-mode shock propagating through a self-gravitating molecular cloud with hourglass-shaped magnetic-field lines. The upper panels show a two-dimensional slice in the x–z-plane, in which the cloud is flattened along the z-direction. The grayscale shading represents the gas density. The blue arrows indicate the velocity field, the magenta curves show the magnetic-field lines, and the orange line represents the shock front. (a) Longitudinal slice of the filament, corresponding to cut R1 in Figure 4. (b) Nearly perpendicular slice of the filament, corresponding to cut R2. The velocity v^* denotes the velocity in the shock rest frame.

shaped magnetic field, where shock compression amplifies the tangential magnetic component and locally bends the field lines. In the upstream region ($z \approx 0.8$–1.0 pc), the magnetic field is oriented parallel to the filament surface and perpendicular to the velocity vectors in the shock rest frame. In contrast, within the dense filamentary structure and the downstream region ($z \lesssim 0.7$ pc), the field lines thread the filament and align parallel to the velocity vectors. These features indicate that the interaction between the fast-mode shock and the curved magnetic field redirects the gas flow and channels the postshock gas along the field lines, forming the radially aligned filament, as schematically illustrated in Figure 5(a).

Figure 4(R2) presents the distributions of density, velocity, and magnetic fields in a slice across the multiple filaments. The density map reveals a corrugated high-density layer, where the gas density is locally enhanced along the mountain-like ridges in the z-direction. These ridges spatially correspond to the filament positions identified in Figure 2(a). This corrugated structure reflects the growth of instabilities resembling the Richtmyer–Meshkov instability, triggered by the shock impact on the weakly turbulent cloud. The magnetic field and velocity structures across this corrugated layer are consistent with those seen in the slice along the filament axis (R1). In the upstream region, the magnetic field is oriented parallel to the corrugated layer and perpendicular to the velocity vectors in the shock rest frame. In contrast, in the downstream region, the field lines thread the layer and align parallel to the velocity vectors, which exhibit a converging flow toward the mountain-like ridges. These features suggest that the gas is not compressed uniformly across the shock plane but is locally accumulated along the corrugations—originating from weak density inhomogeneity—thereby forming the multiple radially aligned filaments (see Figure 5(b)).

4. Discussion

We show that the interaction of a fast-mode shock with a molecular cloud, characterized by an hourglass-shaped

magnetic field bent by self-gravity and density inhomogeneity, forms a radially aligned filament system via a novel formation pathway. This setup, while simplified, corresponds to a physically motivated scenario where a shock (e.g., from a supernova remnant or an expanding H II region) impacts a dense cloud ($n_{\rm H_2} \sim 10^3$–$10^4\,{\rm cm^{-3}}$; e.g., S.-i. Inutsuka et al. 2015). While previous studies have shown that shocks propagating perpendicular to the magnetic field create complex, disordered filamentary density structures (T. Inoue et al. 2018), our results highlight the critical role of the preexisting field geometry. Even with a shock propagating globally parallel to the background field, the hourglass geometry induces an oblique interaction with the curved field lines. This generates a distinct radially aligned morphology, in contrast to the random structures driven by turbulence. Notably, despite this global morphological difference, the local magnetic-field lines still thread the individual filaments, consistent with the local properties reported by T. Inoue et al. (2018) and D. Abe et al. (2021). We also examined models in which the shock is not initially parallel to the magnetic field and found that radially aligned filaments still develop (Figure 1, right panels), although the overall symmetry becomes weaker with increasing inclination. For an isotropic distribution of shock incidence directions, the probability that a shock arrives within an angle ψ (for $\psi < 90°$) of the magnetic-field axis (counting both $\pm$ directions) is $1 - \cos\psi$. For example, this gives $\sim$13% for $\psi = 30°$, indicating that moderately aligned configurations are not exceedingly rare. These results indicates that the formation of an HFS does not require a perfectly aligned shock-field configuration.

The morphology of the radially aligned filaments formed in our simulation closely resembles the HFSs observed in star-forming regions (e.g., M. S. N. Kumar et al. 2020, 2022; D. Arzoumanian et al. 2022; L. K. Dewangan et al. 2025). The filament lengths (1–3 pc) and mean column densities ($\sim 10^{22}\,{\rm cm^{-2}}$) are qualitatively consistent with observed values (e.g., D. Arzoumanian et al. 2022; M. S. N. Kumar et al. 2022). The measured filament width (0.06–0.08 pc) is comparable to, though slightly smaller than, the characteristic $\sim$0.1 pc width reported for nearby star-forming filaments (e.g., D. Arzoumanian et al. 2019). Although HFSs with different spatial scales are also known (e.g., M. S. N. Kumar et al. 2022; L. K. Dewangan et al. 2025), these variations can likely be explained by differences in initial cloud properties (mass and size) and shock parameters (arrival frequency and speed). We note that the mean filament line mass obtained in the present simulation ($\sim 22\,M_\odot\,{\rm pc^{-1}}$) is significantly lower than the values reported in massive protocluster HFSs such as G351.77-0.53 and G012.80, where line masses of $\sim 10^3$–$10^4\,M_\odot\,{\rm pc^{-1}}$ have been measured (e.g., S. D. Reyes-Reyes et al. 2024; J. Salinas et al. 2025). Our model represents either a lower-mass cloud environment compared to massive protocluster HFSs or an earlier evolutionary stage of such systems. The underlying shock–magnetic interaction mechanism is expected to operate over a broad range of cloud masses and shock strengths and may extend to systems with higher filament line masses. A comprehensive study on these dependencies, including the effects of cloud geometry and shock incidence angle, will be presented in a forthcoming Letter.

Regarding kinematics, Figure 3 shows that high-density gas exhibits larger inward radial velocities toward the hub center, whereas the ambient low-density gas retains low radial velocities. This trend is consistent with the kinematic features of observed HFSs (e.g., N. Peretto et al. 2023; N. K. Bhadari et al. 2025). While M. S. N. Kumar et al. (2022) attributed the filament alignment to the gravitational potential of the hub, our results indicate that high-density filaments become radially aligned and selectively exhibit inflow motions immediately after the shock passage. This selective inflow suggests that the observed alignment is driven primarily by the interaction between the external shock and the magnetic-field structure, rather than self-gravity. This kinematic segregation is also reflected in the observationally motivated PV diagram (Figures 3(c1) and (c2)), where the dense filamentary components trace a clear V-shaped structure. The overall PV morphology closely resembles the V-shaped signatures reported in recent high-resolution studies (e.g., R. H. Álvarez-Gutiérrez et al. 2024; J. Salinas et al. 2025; N. A. Sandoval-Garrido et al. 2025), indicating that such kinematic patterns can arise from shock–magnetic field interactions without requiring hub-dominated gravitational focusing.

Our model also provides a simple observational prediction for the projected magnetic-field morphology in HFSs. In the postshock dense filamentary region, the magnetic field exhibits refraction and local enhancement due to oblique fast-mode compression of the hourglass-shaped field. As shown in Figure 4, the field lines thread the filaments and tend to align with the gas flow in the downstream region. The projected orientation of the magnetic field relative to the filament axis depends on the viewing geometry. When viewed from a direction perpendicular to the shock propagation (i.e., along the x- or y-axis), the projected magnetic field can appear largely perpendicular or oblique to the filament axis (see Figure 4(a)). In contrast, when viewed along the shock propagation direction (i.e., along the z-axis), the amplified tangential components dominate the plane-of-the-sky projection, and the magnetic field may appear preferentially aligned with the filament. Such projection effects may help explain the coexistence of filament-parallel and filament-perpendicular magnetic-field morphologies reported in polarization observations of high-mass star-forming regions (e.g., P. Sanhueza et al. 2021; J. Hwang et al. 2022). A detailed synthetic polarization analysis based on our simulations will be presented in future work.

Finally, we discuss the star formation efficiency (SFE) in the radially aligned filament system. In our simulation, dense gas regions ($n_{\rm H_2} > 1 \times 10^5\,{\rm cm^{-3}}$) are replaced by sink particles, yielding a total sink mass of $1.4 \times 10^3\,M_\odot$ at 0.5 Myr after the shock impact. The total gas mass in the computational domain at this epoch is $1.2 \times 10^4\,M_\odot$. Since a continuous inflow is imposed at the boundary ($z = +5$ pc), the total mass increases with time by continuous mass supply into the domain. Assuming a core-to-star conversion efficiency of $\sim 1/3$ (M. N. Machida & T. Matsumoto 2012), the SFE at this epoch is estimated to be 4%. This value is already consistent with the typical SFEs observed in nearby molecular clouds (e.g., N. J. Evans et al. 2009; C. J. Lada et al. 2010) but might be slightly overestimated because of the relatively low-density threshold for sink particle creation in Eulerian grid-based simulations. We expect that simulations with much higher spatial resolution and much higher density threshold for sink creation may reduce the total mass of the sink particles. The total filament mass as illustrated in Figure 2(a) is $1.8 \times 10^3\,M_\odot$. This mass is computed by integrating the

column density over the full filament network identified with DisPerSE, adopting the measured characteristic width, and includes both the prominent central filaments and lower-contrast structures distributed throughout the cloud. The resulting filament mass fraction is 14%, comparable to the observed fraction of 10%–20% in nearby molecular clouds (D. Arzoumanian et al. 2019). Considering that 15% of filament mass typically evolves into prestellar cores (e.g., P. André et al. 2010; V. Könyves et al. 2015) and applying the 1/3 conversion factor (M. N. Machida & T. Matsumoto 2012), the potential SFE of the filamentary dense gas is estimated to be roughly 0.7%. As shown in Figure 3, the ambient low-density gas retains significantly lower radial velocities compared to the dense gas. Kinematic segregation limits the rapid mass supply to the central dense region, thereby preventing an excessively high SFE and limiting SFE.

5. Summary

We have investigated the formation of HFSs using three-dimensional ideal MHD simulations of a fast-mode shock propagating into a molecular cloud characterized by an hourglass-shaped magnetic field and density inhomogeneity. Our results are summarized as follows:

1. The shock–cloud interaction forms a parsec-scale HFS (1–3 pc) consisting of multiple filaments radially aligned toward a central hub. The measured filament width is 0.06–0.08 pc, and the corresponding mean line mass ($22\,M_{\odot}\,\mathrm{pc}^{-1}$) is slightly above the thermal critical value at 10 K. Statistical analysis confirms a strong radial alignment of the filaments, with deviation angles significantly smaller than those expected for a random orientation. Moderate misalignment between the shock direction and the magnetic-field axis weakens the symmetry but does not suppress the formation of radially aligned filaments.
2. The velocity structure of the system exhibits a clear segregation between dense and diffuse gas. Driven by the shock–cloud interaction, high-density gas within the filaments displays inflow velocities increasing toward the hub center, whereas ambient low-density gas retains low radial velocities. This indicates that mass accretion is channeled through the dense filamentary network.
3. The filament formation is driven by the interaction between the planar shock and the curved magnetic field. The oblique shock generated at the bent field lines amplifies the tangential magnetic component, inducing a magnetically guided inflow. The growth of instabilities resembling Richtmyer–Meshkov modes at the shock interface promotes the fragmentation of the shock-compressed layer into multiple filaments.
4. The estimated SFE is 4%, consistent with observations of nearby molecular clouds, but might be reduced in future simulations with higher spatial resolution. The potential SFE in filamentary gas is estimated to be only 0.7%. These results suggest that the kinematic segregation described above limits the rapid mass supply to the central dense region, thereby preventing an excessively high SFE and naturally regulating star formation.

Acknowledgments

We are deeply grateful to Izumi Seno for many insightful discussions throughout this work. We also thank Tomoaki Matsumoto for his major contributions to the code development and Hajime Fukushima and Masahiro Machida for their helpful comments. Numerical simulations in this Letter were conducted by the Cray XC50 (Aterui II) and the Cray XD2000 (Aterui III) at the Center for Computational Astrophysics of National Astronomical Observatory of Japan and the Yukawa-21 at the Yukawa Institute for Theoretical Physics (YITP), Kyoto University. This work was supported in part by MEXT/JSPS KAKENHI grant No. JP25H00394 (S.I.) and JST SPRING grant No. JPMJSP2136 (S.N.). We acknowledge the use of OpenAI's ChatGPT and Google's Gemini only as grammar checking and editing tools to improve the clarity and readability of the manuscript.

Software: DisPerSE (T. Sousbie 2011; T. Sousbie et al. 2011), Astropy (Astropy Collaboration et al. 2013, 2018, 2022), Numpy (C. R. Harris et al. 2020), Matplotlib (J. D. Hunter 2007).

ORCID iDs

Shingo Nozaki https://orcid.org/0000-0003-4271-4901
Shu-ichiro Inutsuka https://orcid.org/0000-0003-4366-6518

References

Abe, D., Inoue, T., Inutsuka, S.-i., & Matsumoto, T. 2021, ApJ, 916, 83
Álvarez-Gutiérrez, R. H., Stutz, A. M., Sandoval-Garrido, N., et al. 2024, A&A, 689, A74
André, P., Men'shchikov, A., Bontemps, S., et al. 2010, A&A, 518, L102
Arzoumanian, D., André, P., Könyves, V., et al. 2019, A&A, 621, A42
Arzoumanian, D., Russeil, D., Zavagno, A., et al. 2022, A&A, 660, A56
Astropy Collaboration, Price-Whelan, A. M., Lim, P. L., et al. 2022, ApJ, 935, 167
Astropy Collaboration, Price-Whelan, A. M., Sipőcz, B. M., et al. 2018, AJ, 156, 123
Astropy Collaboration, Robitaille, T. P., Tollerud, E. J., et al. 2013, A&A, 558, A33
Beltrán, M. T., Padovani, M., Girart, J. M., et al. 2019, A&A, 630, A54
Bhadari, N. K., Dewangan, L. K., Jadhav, O. R., et al. 2025, A&A, 694, L18
Crutcher, R. M., Wandelt, B., Heiles, C., Falgarone, E., & Troland, T. H. 2010, ApJ, 725, 466
Dewangan, L. K., Bhadari, N. K., Maity, A. K., et al. 2025, AJ, 169, 80
Evans, N. J., II, Dunham, M. M., Jørgensen, J. K., et al. 2009, ApJS, 181, 321
Fukushima, H., & Yajima, H. 2021, MNRAS, 506, 5512
Fukushima, H., Yajima, H., Sugimura, K., et al. 2020, MNRAS, 497, 3830
Harris, C. R., Millman, K. J., van der Walt, S. J., et al. 2020, Natur, 585, 357
Heyer, M., & Dame, T. M. 2015, ARA&A, 53, 583
Hunter, J. D. 2007, CSE, 9, 90
Hwang, J., Kim, J., Pattle, K., et al. 2022, ApJ, 941, 51
Inoue, T., Hennebelle, P., Fukui, Y., et al. 2018, PASJ, 70, S53
Inutsuka, S.-i., Inoue, T., Iwasaki, K., & Hosokawa, T. 2015, A&A, 580, A49
Kashiwagi, R., Iwasaki, K., & Tomisaka, K. 2024, ApJ, 974, 265
Könyves, V., André, P., Men'shchikov, A., et al. 2015, A&A, 584, A91
Kumar, M. S. N., Arzoumanian, D., Men'shchikov, A., et al. 2022, A&A, 658, A114
Kumar, M. S. N., Palmeirim, P., Arzoumanian, D., & Inutsuka, S. I. 2020, A&A, 642, A87
Lada, C. J., Lombardi, M., & Alves, J. F. 2010, ApJ, 724, 687
Machida, M. N., & Matsumoto, T. 2012, MNRAS, 421, 588
Matsumoto, T. 2007, PASJ, 59, 905
Matsumoto, T., Dobashi, K., & Shimoikura, T. 2015, ApJ, 801, 77
Myers, P. C. 2009, ApJ, 700, 1609
Nozaki, S., Fukushima, H., Tokuda, K., & Machida, M. N. 2025, ApJ, 980, 101
Pattle, K., Fissel, L., Tahani, M., Liu, T., & Ntormousi, E. 2023, ASPC, 534, 193

Peretto, N., Fuller, G. A., André, P., et al. 2014, A&A, 561, A83
Peretto, N., Rigby, A. J., Louvet, F., et al. 2023, MNRAS, 525, 2935
Reyes-Reyes, S. D., Stutz, A. M., Megeath, S. T., et al. 2024, MNRAS, 529, 2220
Salinas, J., Stutz, A. M., Álvarez-Gutiérrez, R. H., et al. 2025, arXiv:2510.03447
Sandoval-Garrido, N. A., Stutz, A. M., Álvarez-Gutiérrez, R. H., et al. 2025, A&A, 696, A202
Sanhueza, P., Girart, J. M., Padovani, M., et al. 2021, ApJL, 915, L10
Shimajiri, Y., André, P., Ntormousi, E., et al. 2019, A&A, 632, A83
Sousbie, T. 2011, MNRAS, 414, 350
Sousbie, T., Pichon, C., & Kawahara, H. 2011, MNRAS, 414, 384
Treviño-Morales, S. P., Fuente, A., Sánchez-Monge, Á., et al. 2019, A&A, 629, A81
Vázquez-Semadeni, E., Palau, A., Gómez, G. C., et al. 2025, MNRAS, in press,
Wang, J.-W., Koch, P. M., Galván-Madrid, R., et al. 2020a, ApJ, 905, 158
Wang, J.-W., Lai, S.-P., Clemens, D. P., et al. 2020b, ApJ, 888, 13
Wang, J.-W., Lai, S.-P., Eswaraiah, C., et al. 2019, ApJ, 876, 42
Zhou, J. W., Wyrowski, F., Neupane, S., et al. 2023, A&A, 676, A69